

# Physical and Mechanical Characterization of $\text{Ti}_{50}\text{Ni}_{(50-x)}\text{Fe}_x$ Shape Memory Alloy Fabricated by Spark Plasma Sintering Process



JAGADISH PARIDA, SUBASH CHANDRA MISHRA,  
DEEPAK KUMAR SATAPATHY, KISHORE KUMAR BEHERA, and AJIT BEHERA

NiTi smart alloys are known for their characteristic shape memory behavior. The current work focuses on the physical and mechanical characterization of  $\text{Ni}_{(50-x)}\text{Ti}_{50}\text{Fe}_x$  shape memory alloys prepared by the spark plasma sintering (SPS) process and their dependence on the concentration of Fe. The physical characterization of the samples confirmed the presence of the FeNiTi phase along with the Ti- and Ni-rich phases. Enhanced mechanical properties were observed in 8 at. pct Fe samples, which contained secondary intermetallic phases such as  $\text{Ti}_2\text{Ni}$ ,  $\text{Ni}_3\text{Ti}$ ,  $\text{Fe}_2\text{Ti}$ , and  $\text{Ni}_4\text{Ti}_3$ . Higher fraction of NiTi phase in the 8 at. pct Fe sample resulted in better shape memory properties while showing a higher friction coefficient. Ball on disk wear tests were done to identify the mechanisms contributing to the wear in the sintered sample. It is observed that the abrasive wear as well as the adhesive wear are the most prominent contributors for the surface material removal, and the dependence of characterization is observed with the variation of Fe content in NiTiFe alloy.

<https://doi.org/10.1007/s11661-024-07562-x>

© The Minerals, Metals & Materials Society and ASM International 2024

## I. INTRODUCTION

IN the past few decades, shape memory alloys have garnered significant attention owing to their applications across diverse fields, from naval to aerospace industries, medical implantation to surgical instruments, etc.<sup>[1–3]</sup> The most recognized of the well-known SMAs is NiTi, which has a remarkable combination of high flow stress along with considerable shape memory effect strain.<sup>[1]</sup> The NiTiFe (NiTi-based) alloy possesses a high melting point of 1320 °C; the production of NiTiFe alloys is fabricated using both the powder metallurgy route and the melting/casting route. Numerous PM methods, namely, Self-propagating high-temperature synthesis, conventional sintering, spark plasma sintering, selective laser melting, and microwave sintering, have been employed to manufacture NiTiFe alloys.<sup>[4–8]</sup> But the SPS technique has gained prominence as the most efficient sintering method for alloys and metals, as

it boasts a remarkable ability for densification while keeping grain growth to a minimum.<sup>[9]</sup> Also, it is suitable for controlling the homogeneity, composition, and density with a lower sintering temperature and shorter processing time.<sup>[10]</sup> However, these powder metallurgy methods have certain limits because of their complexity and susceptibility to oxidation, which can lead to the formation of various undesirable phases such as  $\text{NiTi}_2$ ,  $\text{TiNi}_3$ , and  $\text{Ni}_4\text{Ti}_3$  because of composition fluctuations in the specimens.<sup>[5,6,8,11,12]</sup> In general, a material composed entirely of the NiTi phase exhibits excellent high mechanical properties, making it suitable for medical implantation and surgical uses.<sup>[13]</sup> On the other hand, the presence of  $\text{Ti}_2\text{Ni}$  and  $\text{TiNi}_3$  phases in NiTi may make the implants more brittle.<sup>[14]</sup> When the chemical composition of NiTi alloys exceeds Ti-50 at. pct Ni, it results in precipitation in the Ni-rich region, particularly  $\text{Ni}_4\text{Ti}_3$  within the B2 matrix.<sup>[15]</sup> These fine precipitates of  $\text{Ni}_4\text{Ti}_3$  play a crucial role in enhancing the austenitic strength and restricting the extent of plastic deformation during martensitic transformation, especially under cyclic loading or temperature conditions.<sup>[16]</sup> The  $\text{Ni}_4\text{Ti}_3$  precipitates presence results in the development of strain fields that contribute to improved shape memory recoverability. In comparison to near equiatomic TiNi alloy, Ni-rich shape memory alloys exhibit higher hardness values owing to the mechanism of precipitation hardening, which increases the critical stress required for slip.<sup>[16]</sup> Finally,

JAGADISH PARIDA, SUBASH CHANDRA MISHRA, DEEPAK KUMAR SATAPATHY, and AJIT BEHERA are with the Metallurgical and Materials Engineering Department, National Institute of Technology, Rourkela, Odisha, 769008, India. Contact e-mail: beheraajit@nitrkl.ac.in KISHORE KUMAR BEHERA is with the Metallurgical and Materials Engineering Department, Indian Institute of Technology Madras, Chennai, 600036, India. Manuscript submitted December 21, 2023; accepted August 20, 2024.

the importance of phases is desirable or undesirable depending on the application of the alloy.

Fe is added to the NiTi system as a cost-effective substitution for Ni. Fe addition introduces many desirable properties, such as low-temperature hysteresis, higher toughness, higher corrosion resistance, radiopacity, and lower martensitic phase transformation temperatures.<sup>[17]</sup> As a result, NiTiFe alloys find usage in a wide range of engineering applications, such as heat-shrinkable hydraulic couplings and sleeves in the aeronautical industry due to their low martensitic temperature.<sup>[18]</sup> Fe addition to the NiTi system also reduces the transformation temperature and forms an intermediate R-phase between the martensite and austenite phases.

NiTi-based alloys are known to possess enhanced resistance to wear.<sup>[19–21]</sup> Prior investigations on the wear resistance of TiNi-based alloys in various wear conditions showed that the observed wear resistance was significantly better than conventional materials such as steel, Ni-based and Co-based alloys.<sup>[21–23]</sup> The wear resistance of any conventional material has a strong dependence on the mechanical properties, such as work-hardening and hardness.<sup>[24]</sup> However, in the case of TiNi-based alloys, mechanical properties along with the shape memory behavior are responsible for the high wear resistance. The wear resistance of TiNi-based alloys was found to be 10–30 times better than pure Ni and Ti during the sliding wear tests conducted in dry conditions.<sup>[25]</sup> Abrasion and delamination of sub-surface cracks were found to be the prominent mechanisms prevalent in these alloys during cyclic loading.

There is no paper on the NiTiFe smart alloy prepared by spark plasma sintering. Here, the papers focused on the investigation of the physical and mechanical characterization of the NiTiFe specimens prepared by the spark plasma sintering process. Interestingly, the dependence of characterization was observed with the variation of Fe content in NiTiFe alloy.

## II. MATERIALS AND METHODS

Elemental Powders of Ni (purity: > 99.8 pct, particle size: 74–100  $\mu\text{m}$ ), Fe (purity: > 99.5 pct, particle size: 6–10  $\mu\text{m}$ ), and Ti (purity: > 99 pct, particle size: < 45  $\mu\text{m}$ ), respectively, were purchased from Alfa Aesar, U.S.A. for the study. The powders were mixed in a tubular mixture (Willy A. Bachofen AG, Maschinenfabrik, Switzerland) for 12 h in the desired proportion of  $\text{Ni}_{(50-X)}\text{Ti}_{50}\text{Fe}_X$  (where  $X = 0, 2, 4, 6, 8,$  and  $10$  in at. pct) to achieve homogenization followed by sintering in a spark plasma sintering unit (Dr. Sinter, Model SPS-625, SPS Syntex Inc.) at 1000 °C for 5 min holding

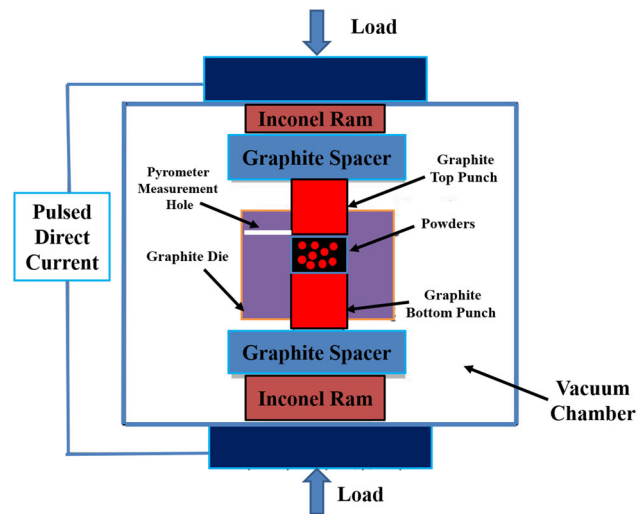


Fig. 1—Schematic diagram of the SPS instrument.

time and 50 MPa applied pressure at a heating rate of 50 °C/min. Figure 1 shows a schematic diagram of the SPS instrument. The other process parameters, such as 4.5 volt voltage, 1200 ampere current, less than 10 Pa vacuum level, and 100 °C/min cooling rate, are used. A cylindrical graphite die with an inner diameter of 15 mm was used. The specimens are identified by the amount of Fe in the system: an alloy containing 2 at. pct Fe is represented as 2Fe in the text. The sintered specimens (diameter: 15 mm and thickness: 6 mm) were polished prior to their physical and mechanical characterization.

Physical characterization measurement systems like X-ray diffraction (BRUKER model: D8 ADVANCE XRD) were used for phase analysis, while SEM-EDS (make: JEOL, model: JSM-6480LV) was used for microstructural and composition analysis. A Co target (Co  $K\alpha = 0.179$  nm) was used for the X-ray diffraction process with constant parameters (*i.e.*,  $2\theta$  range 30–120 deg, scan rate: 5°/min, and step size: 0.02). For measuring the density and porosity by Archimedes Principle, the sintered specimens were soaked in distilled water for 24 h.<sup>[26]</sup> Nanomechanical properties such as nanohardness, elastic recovery ratio, and elastic modulus were determined from the nanoindentation tests using the Hysitron TI950 TriboIndenter. A load of 8000  $\mu\text{N}$  with a 0.8 mN/sec loading and unloading rate and a holding time of 10 s was employed in the test.<sup>[27]</sup> Eight indents were obtained using a Berkovich diamond indenter on different regions, and the average values were calculated. Vickers microhardness (make: Leco, model: LM248AT) tests were also performed with a load of 500 gf for 10 seconds.<sup>[28]</sup> The hardness values reported are averaged out from at least ten indentations

from different regions of the specimens. To observe the shape memory effect by indentation method (micro-Vickers), a load of 1 Kg-f for 10 seconds was applied, followed by heating in a vacuum furnace at 100 °C for 1800 seconds. The specimens were furnace cooled prior to the measurement of shape recovery.<sup>[29]</sup> A ball on plate system (make: Ducom, model: TR-208-M1) was used to study the wear behavior of the sintered compacts. A 2-mm-diameter Si<sub>3</sub>N<sub>4</sub> ball was used at 30 N load and 30 rev/min sliding speed for 10 minutes.<sup>[30]</sup> The following formula using Eqs. [1] and Eq [2] was adopted for calculating the shape memory effect<sup>[29]</sup> and the elastic recovery ratio from the load-depth curve.<sup>[31]</sup>

$$\text{Shape Memory Effect} = \frac{D_1 - D_2}{D_1} * 100 \quad [1]$$

$$\text{Elastic recovery ratio} = \frac{D_{\max} - D_r}{D_{\max}}, \quad [2]$$

where  $D_2$  and  $D_1$  are the average values ( $\mu\text{m}$ ) of indentation of the sample after and before heating, respectively. Also,  $D_{\max}$  and  $D_r$  are the maximum indentation depth and the residual depth, respectively.

### III. RESULTS AND DISCUSSION

#### A. Powder Characterization

Figure 2(a) shows the elemental mapping of the 4Fe powder mixture. It is observed that spherical particles are Ni powder, and irregular-shaped particles are Ti and Fe powder. The average particle size of Ni, Ti, and Fe powders are less than 100, 45, and 10  $\mu\text{m}$ , respectively. Also, individual elements are represented by different colors, and uniformly distributed elements show that uniform mixing has been achieved. Figure 2(b) shows the typical histogram of particle size distribution for the 4Fe powder mixture, as determined by particle size analysis. The histogram shows bell-shaped curves or

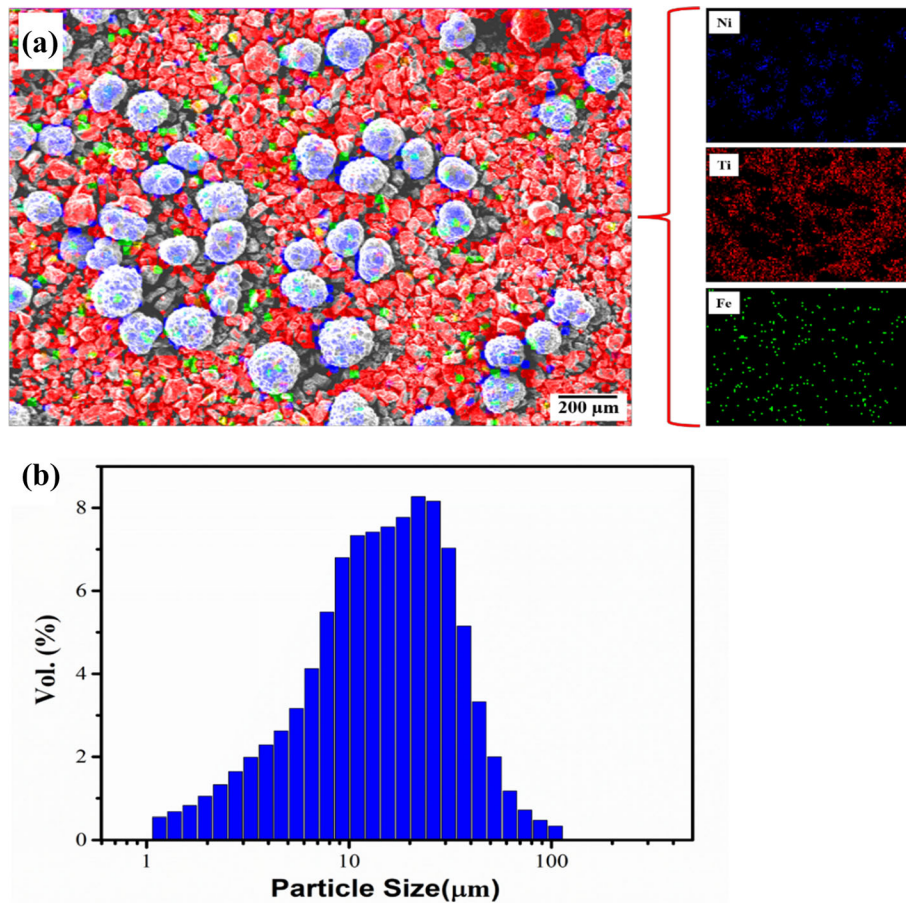


Fig. 2—(a) Elemental mapping and (b) particle size analysis of 4Fe powder mixture.

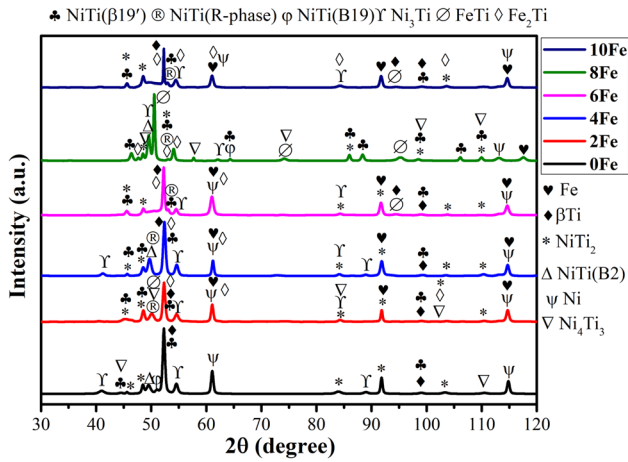


Fig. 3—XRD analysis of different composition samples.

Gaussian distribution, and mixed powder has a wide size distribution of about 10–100  $\mu\text{m}$ .

### B. Phase and Microstructural Analysis

Phases such as NiTi and FeTi, along with many secondary phases like  $\text{Ti}_2\text{Ni}$ ,  $\text{TiNi}_3$ ,  $\text{Fe}_2\text{Ti}$ , and  $\text{Ti}_3\text{Ni}_4$ , were detected from the X-ray diffraction results of all compositions of samples in Figure 3, showed that a various number of intermetallic phase formation take place after the SPS process. Table I provides the phases present in each sample, along with their corresponding reference codes from Figure 3. As known, there is always a possibility of getting multiple phases when dealing with shape memory alloys based on NiTi.<sup>[32]</sup> The NiTi(B19') phase in more amounts is present in 8Fe composition samples (as observed in many peaks in Figure 3). However, in the rest composition of the samples, it is present in less amount. The NiTi (B19') and FeTi phases are known to possess superelastic behavior, whereas the secondary phases (such as  $\text{Ti}_2\text{Ni}$ ,  $\text{TiNi}_3$ ,  $\text{Ni}_4\text{Ti}_3$ , and  $\text{Fe}_2\text{Ti}$ ) influence the hardness and tribological behavior of the specimens.<sup>[33]</sup>

Scanning electron micrographs were obtained in backscattered mode (provided good compositional contrast) to clearly differentiate between the various phases present in the microstructure, with heavier elements appearing brighter due to strong backscattered electron emission. The different phases formed appeared in the sequence from dark to bright of  $\beta\text{Ti}$ ,  $\text{Ti}_2\text{Ni}$  or  $(\text{Ni}, \text{Fe})\text{Ti}_2$ , TiNi or NiFeTi,  $\text{TiNi}_3$ ,  $\text{Fe}_2\text{Ti}$ , and Ni on a gray

scale. However, the contrast between  $\text{Fe}_2\text{Ti}$  and  $\text{Ni}_3\text{Ti}$  was too weak to distinct visually under SEM, requiring EDS analysis for phase identification. SEM images of the sample are presented in Figure 4. As depicted in the micrograph in lower magnification, the sample displayed only white and dark regions. Furthermore, the magnified micrograph indicates the formation of an intermediate phase with a mid-scale contrast positioned between the white and dark phases.

The elemental compositions of the phases marked in Figure 4 are presented in Table II. It is worth noting that the white regions do not contain pure Ni or Fe but rather a Ni/Fe solid solution with a few atomic percentages of Ti. On the other hand, the dark regions are predominantly composed of Ti, with a few atomic percent of Ni or Fe. The Ni/Fe phase exists as isolated islands, while Ti forms a continuous structure. The formation of  $\text{Ti}_2\text{Ni}$  seems to have occurred along the interface of the Ni particles, resulting from the diffusion of Titanium into Nickel. This observation suggests that the sintering process commenced at 1000  $^\circ\text{C}$ . It is worth noting that this temperature surpasses the eutectic point at 942  $^\circ\text{C}$  in the NiTi phase diagram, so localized melting is possible in the course of sintering. In the given sintered sample, only five phases were present, including  $\beta\text{-Ti}$ ,  $\text{Ti}_2\text{Ni}$  or  $(\text{Ni}, \text{Fe})\text{Ti}_2$ , TiNi or NiFeTi,  $\text{TiNi}_3$ ,  $\text{Fe}_2\text{Ti}$ , and Ni. Notably, Ti had completely disappeared, as shown in the micrograph of the 8Fe sample, where the dark black regions correspond to voids. The formation of  $\text{TiNi}_3$  occurred close to Ni, while  $\text{Ti}_2\text{Ni}$  was formed next to Ti. In between  $\text{TiNi}_3$  and  $\text{Ti}_2\text{Ni}$ , the network of TiNi is formed that extends toward the Ti phase. Through EDS analysis also, it is found that the two types of Ti solid solutions, namely  $\beta\text{-Ti}$ , are present in the sample. The dark gray regions indicated  $\beta\text{-Ti}$  with 92.68 at. pct Ti and  $\beta\text{-Ti}$  with 82.44 at. pct Ti. Within the 8Fe specimen, the TiNi network had consolidated into a continuous matrix in most areas, while small rounded islands of  $\text{Ti}_2\text{Ni}$  were trapped inside the TiNi matrix, as illustrated in the micrograph of the 8Fe sample. Moreover, thin veins of  $\text{TiNi}_3$  forming a network appeared within the NiTi matrix. These veins of  $\text{TiNi}_3$  followed the TiNi grain boundaries. Needle-like structures, which are thin disks and are thought to be  $\text{Ti}_3\text{Ni}_4$  precipitates, have also appeared within the TiNi matrix. These structures are generally  $\text{Ti}_3\text{Ni}_4$  phase with the average nickel content of 56–60 at. pct and Ti content of 37–40 at. pct with few amount of iron content.

**Table I. The XRD Peaks' Details are in Fig. 3**

Compound Name	Chemical Formula	$2\theta$ (degree)	d-spacing [ $\text{\AA}$ ]	(h k l)	Reference Code
Nickel Titanium (R-phase)	NiTi	50.091	2.112	(2-12)	98-011-3056
		53.044	2.002	(110)	98-010-2932
Nickel Titanium	NiTi(B19)	51.029	2.076	(111)	98-011-0092
Nickel Titanium (Austenite)	NiTi(B2)	49.541	2.134	(011)	98-009-0782
Nickel Titanium (Martensite)	NiTi(B19')	45.598	2.308	(002)	98-008-0888
		46.402	2.270	(101)	
		48.455	2.179	(11-1)	98-011-4257
		52.482	2.026	(01-2)	98-008-0888
		64.330	1.680	(102)	
		85.989	1.311	(03-1)	
		88.384	1.283	(103)	
		99.044	1.176	(131)	
		106.115	1.119	(13-2)	
		109.961	1.092	(22-2)	
		Iron Titanium (1/1)	FeTi	50.311	2.104
74.153	1.483			(002)	
94.493	1.218			(112)	
Iron Titanium (2/1)	Fe <sub>2</sub> Ti	47.657	2.214	(013)	98-008-8363
		52.322	2.026	(112)	98-008-8354
		53.644	2.003	(021)	98-008-8363
		54.071	1.967	(004)	
Nickel Titanium (1/2)	NiTi <sub>2</sub>	61.065	1.76	(014)	98-008-8354
		45.597	2.308	(224)	98-000-4100
		48.551	2.217	(115)	
		53.044	2.003	(044)	
		84.154	1.334	(066)	
		91.822	1.245	(119)	
Nickel Titanium (3/1)	Ni <sub>3</sub> Ti	103.491	1.139	(177)	
		110.031	1.092	(159)	
		40.998	2.548	(110)	98-001-3097
		49.541	2.134	(021)	
		54.523	1.951	(022)	
		62.074	1.734	(023)	
		84.291	1.331	(025)	
Nickel Titanium (4/3)-Ht	Ni <sub>4</sub> Ti <sub>3</sub>	88.940	1.276	(220)	
		44.503	2.362	(131)	98-012-2611
		48.492	2.178	(401)	
		50.091	2.112	(5-40)	
		57.699	1.853	(330)	
		74.153	1.483	(6-22)	
		84.291	1.331	(351)	
		98.482	1.180	(081)	
		103.671	1.137	(7-53)	
		109.968	1.092	(802)	
Beta-Titanium	$\beta$ -Ti	110.494	1.088	(802)	
		52.257	2.031	(002)	98-002-3322
		94.415	1.219	(113)	
Nickel	Ni	99.082	1.176	(222)	
		61.065	1.760	(020)	96-901-1598
		113.123	1.071	(131)	96-901-3006
Iron	Fe	114.844	1.061	(131)	96-901-1598
		61.014	1.760	(020)	96-901-6481
		91.854	1.245	(022)	
		114.642	1.063	(131)	
		117.573	1.045	(131)	96-901-4114

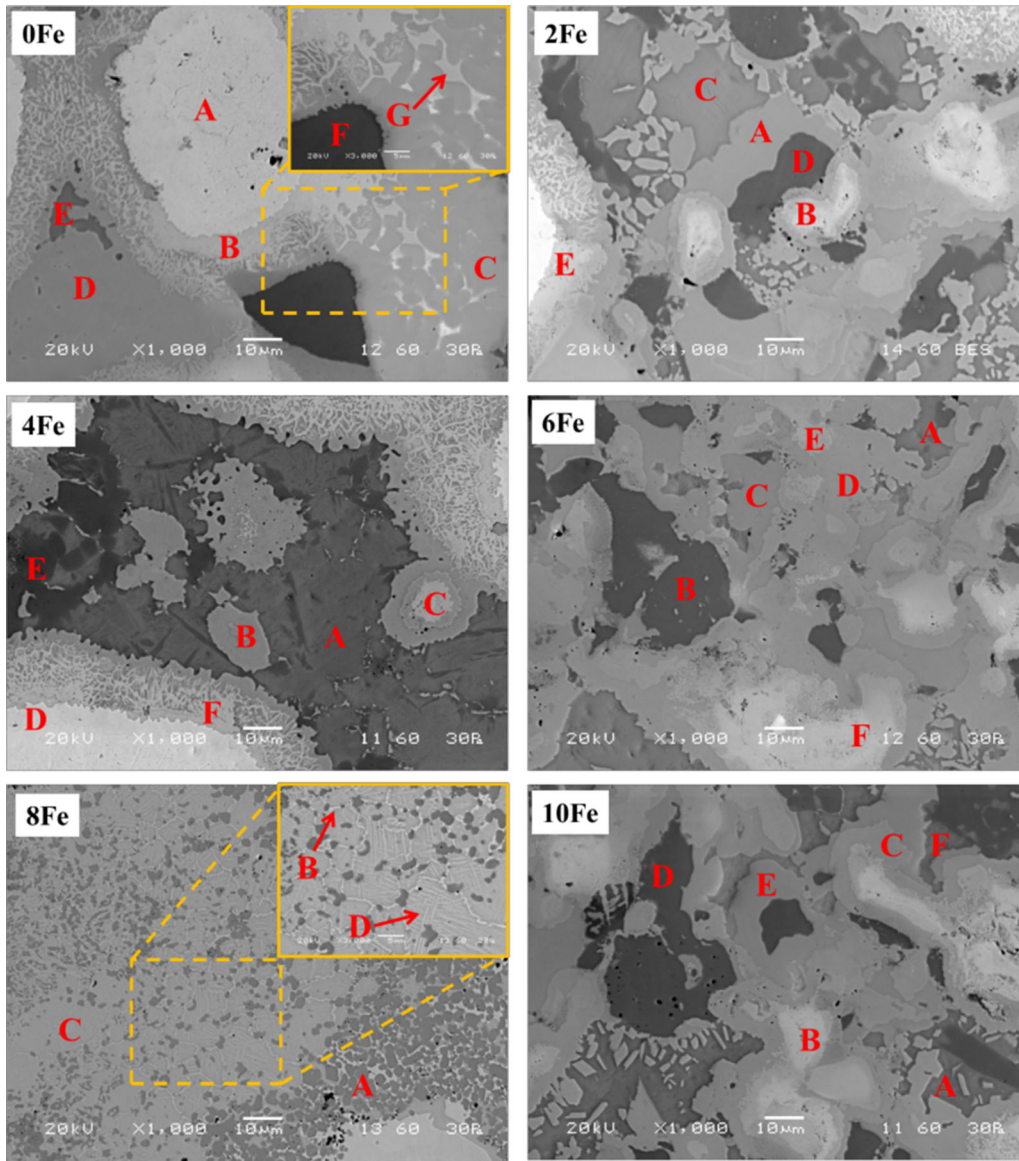


Fig. 4—SEM micrographs of different composition samples.

Figure 5 shows the distribution of Ni, Ti, and Fe in the 4Fe sample. The Ti-rich phase is identified by charcoal gray regions, while the TiNi or TiNiFe and (Fe, Ni)-rich or  $Fe_2Ti$  phases are represented by gray and white regions, respectively. Some micro-pores are seen near or along the Ti-rich or the Ni-rich phase, and

also at the interface between the Ni-rich and Ti-rich phases, which is by the diffusion that results from the Kirkendall effect.<sup>[34,35]</sup> Figure 6(a, b) depicts the line scan analysis of the 2Fe sample across different phases. From the figure, it can be seen how each of these elements varies from the ash gray phase to the white

**Table II. Chemical Compositions of Various Regions are Marked in Fig. 4**

Samples Name	Regions in Micrograph	Composition (at. pct)			Phase
		Ni	Ti	Fe	
0Fe	A	84.60	15.40	—	Ni-rich
	B	49.24	50.27	—	NiTi
	C	32.94	67.06	—	NiTi <sub>2</sub>
	D	10.23	89.77	—	β-Ti
	E	8.33	91.67	—	β-Ti
	F	10.08	89.92	—	β-Ti
	G	47.41	52.49	—	NiTi
2Fe	A	12.47	65.13	22.39	(Ni, Fe)Ti <sub>2</sub>
	B	6.98	30.47	62.55	Fe <sub>2</sub> Ti
	C	8.92	83.46	7.62	β-Ti
	D	8.67	85.36	5.97	β-Ti
	E	42.55	56.49	0.99	NiTi
4Fe	A	10.17	86.37	3.45	β-Ti
	B	28.37	65.33	6.31	(Ni, Fe)Ti <sub>2</sub>
	C	8.98	25.32	65.70	Fe <sub>2</sub> Ti
	D	79.28	16.91	3.81	Ni-rich
	E	9.11	82.44	8.46	β-Ti
	F	45.15	48.04	6.18	(Ni, Fe)Ti
6Fe	A	7.91	88.49	3.60	β-Ti
	B	1.68	92.68	5.63	β-Ti
	C	1.96	75.58	22.47	(Ni, Fe)Ti <sub>2</sub>
	D	2.04	65.26	32.70	(Ni, Fe)Ti <sub>2</sub>
	E	11.88	51.63	36.49	(Ni, Fe)Ti
	F	7.58	27.11	65.31	Fe <sub>2</sub> Ti
	G	18.02	68.39	13.59	(Ni, Fe)Ti <sub>2</sub>
8Fe	B	65.38	28.84	5.78	Ni <sub>3</sub> Ti
	C	35.46	48.96	15.58	(Ni, Fe)Ti
	D	46.19	39.37	14.44	Ni <sub>4</sub> Ti <sub>3</sub>
	E	4.12	83.95	11.93	β-Ti
10Fe	B	7.16	28.79	64.05	Fe <sub>2</sub> Ti
	C	4.23	72.17	23.50	(Ni, Fe)Ti <sub>2</sub>
	D	5.91	88.70	5.40	β-Ti
	E	4.26	44.09	51.65	(Ni, Fe)Ti
	F	4.23	82.41	13.36	β-Ti

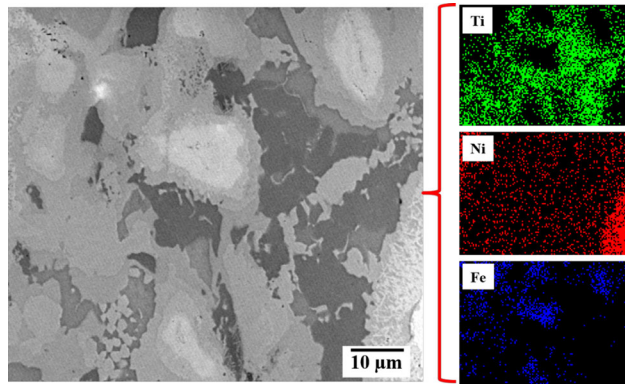


Fig. 5—Elemental mapping of 4Fe sample.

phase through the charcoal gray and gray phases. The ash and charcoal gray region contains more Ti than any other element. Similarly, Fe and Ni are in high amounts in the white region, and Ti is in low amounts, but in the gray phase, Ti elements, along with Ni and Fe elements, are present.

### C. Porosity and Density Measurement

Figure 7 shows the sintered density of all compositions of samples. The density values of different samples (from 0 to 10Fe) are 6.046 gm/cc, 6.081 gm/cc, 5.978 gm/cc, 6.155 gm/cc, 6.191 gm/cc, and 6.127 gm/cc, respectively. It is found that the 8Fe sample has a higher density (6.191 gm/cc) due to a lower porosity

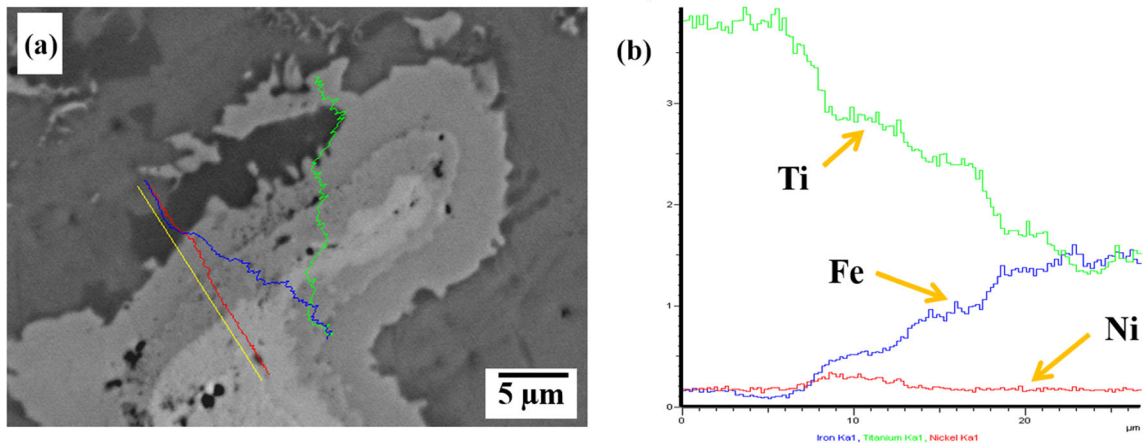


Fig. 6—(a, b) Line scan analysis of different element change concentrations compared to a different phase in the 2Fe sample.

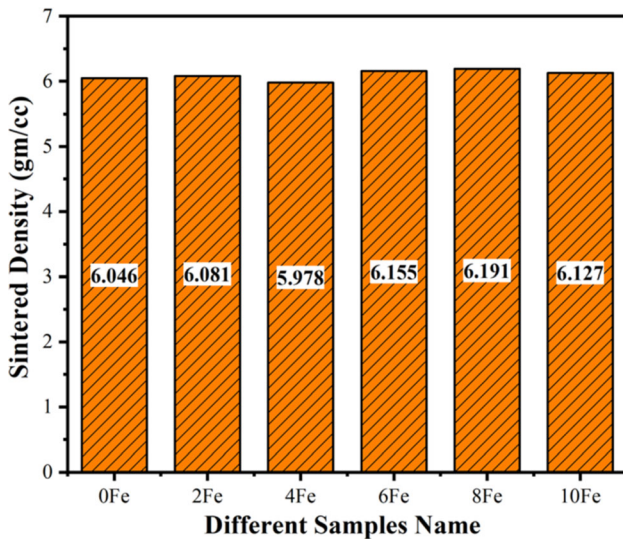


Fig. 7—Sintered density value vs different composition samples.

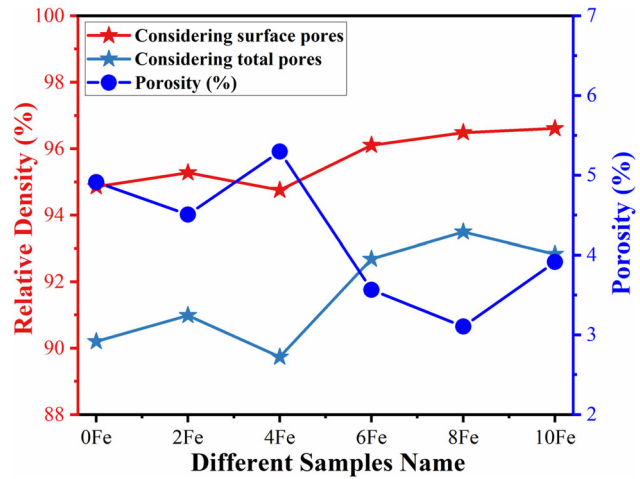


Fig. 8—Graphical representation of Relative density and Porosity vs Fe content.

value or better diffusion of the sample than other composition samples.

Figure 8 presents the variation of relative densities in the specimens when surface pores and total pores are considered. The variation of porosity at different Fe contents is also included in Figure 8. The porosity percentage from relative density based on surface pores and total pores is calculated using the method already mentioned in our previous paper.<sup>[36,37]</sup> It was observed that adding Fe to the NiTi system increases diffusivity, which led to an overall decrease in the porosity values and a higher relative density. Because of that, the 8Fe sample shows the least porosity (3.11 pct) levels among all samples, which is shown in Figure 8 and Table III.

#### D. Shape Memory Effect and Superelasticity Behavior Study

Figure 9 shows the effect of Fe content on the shape memory behavior of the samples. The specimen of 8Fe sample showed the highest shape memory effect (SME), which can be ascribed to the higher fraction of NiTi (B19') is shown in Figure 3 compared to other composition samples. Also, better densification results from the increased diffusion, making the NiTi (B19') and FeTi phases in the 8Fe sample more stable compared to others, as shown in Figures 3 and 7.<sup>[38]</sup> The presence of secondary phases ((Ni, Fe)Ti<sub>2</sub> and Fe<sub>2</sub>Ti) and βTi phases in samples has yet to be investigated for shape



**Table III. Dependence of Porosity (pct) and Relative Density on the Fe Content in the NiTi System**

Sample Name	Relative Density (Surface Pores) (pct)	Relative Density (Total Pores) (pct)	Porosity (pct)
0Fe	94.858	90.199	4.91
2Fe	95.277	90.983	4.51
4Fe	94.751	89.731	5.30
6Fe	96.107	92.681	3.56
8Fe	96.486	93.492	3.11
10Fe	96.609	92.828	3.91

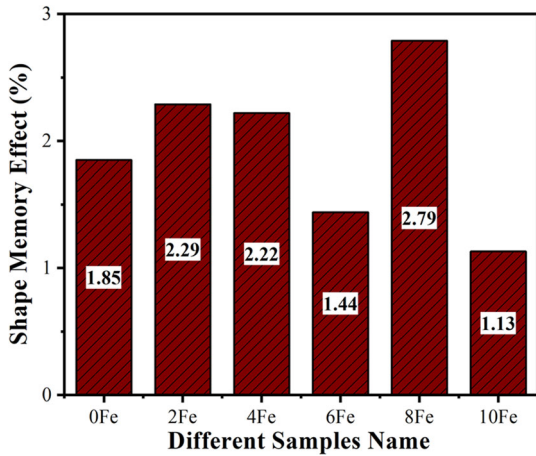


Fig. 9—The shape memory effect of samples with varying Fe contents.

memory behavior, but the existence of intermediate phases like  $\text{NiTi}_2$  and  $\text{Ni}_3\text{Ti}$  does not exhibit shape memory behavior.<sup>[39]</sup> The values of  $D_1$  and  $D_2$  were calculated from the optical micrograph of the 8Fe sample in Figure 10. The calculated  $D_1$  and  $D_2$  values for the specimens are presented in Table IV.

Figure 11(a) shows the load vs depth of indentation curve of all the samples. The elastic recovery ratios (ERR) of different samples (from 0 to 10Fe) are 37.76 pct, 44.97 pct, 38.01 pct, 36.28 pct, 49.22 pct, and 16.19 pct, respectively, as shown in Figure 11(c). From the figure, one can see that the elastic recovery of 8Fe is the highest while that of 10Fe is the lowest. Higher elastic recovery values of certain specimens can be attributed to the presence of NiTi martensitic phase ( $\text{B19}'$ ), while the presence of secondary phases can fluctuate the recovery ratio.<sup>[40]</sup> The average hardness, as well as elastic modulus values as a function of Fe content, are plotted in Figure 11(b). It was found that the 8Fe sample showed higher nanohardness and elastic

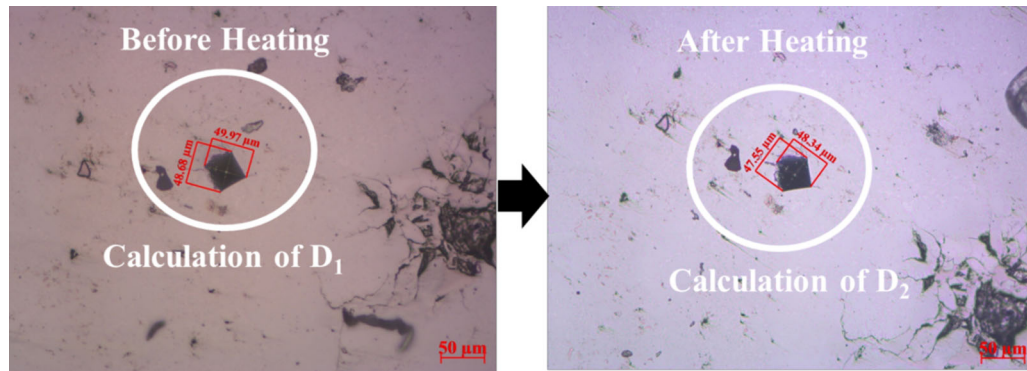


Fig. 10—An optical micrograph of 8Fe sample.

modulus as compared to other compositions; higher amounts of  $\text{Ni}_3\text{Ti}$ ,  $\text{Ni}_4\text{Ti}_3$ ,  $\text{Fe}_2\text{Ti}$ , and  $\text{NiTi}_2$  phases could be a reason behind higher hardness values.<sup>[41]</sup> These intermetallics can play a major role in enhancing the elastic modulus and nanohardness of the specimens way better than the  $\text{TiNi}$  intermetallic phase.<sup>[42]</sup>

### E. Hardness and Tribological Study

Figure 12 shows the average hardness values of different samples. The hardness values of different samples (from 0 to 10Fe) are 432.18 VHN, 600.2 VHN, 416.67 VHN, 720.82 VHN, 817.8 VHN, and 658.47 VHN, respectively. The reason behind the higher hardness value of the 8Fe specimen is due to the level of densification achieved during the SPS process

**Table IV. Shape Memory Effect Properties of Samples**

Sample Name	$D_1$ ( $\mu\text{m}$ )	$D_2$ ( $\mu\text{m}$ )	SME (pct)
0Fe	64.715	63.515	1.854
2Fe	81.605	79.735	2.292
4Fe	72.545	70.935	2.22
6Fe	54.845	54.055	1.44
8Fe	49.325	47.945	2.794
10Fe	64.9	64.17	1.125

(Figure 7). Also, the presence of hard intermetallic phases ( $\text{Ni}_4\text{Ti}_3$ ,  $\text{Ni}_3\text{Ti}$ , and  $\text{NiTi}_2$  precipitates) in the 8Fe contributes to higher hardness values, as shown in Figures 3 and 4.<sup>[38,43]</sup>

Figure 13(a, b) shows the variation of wear depth and coefficient of friction in comparison to the sliding distance. The friction coefficient variation in

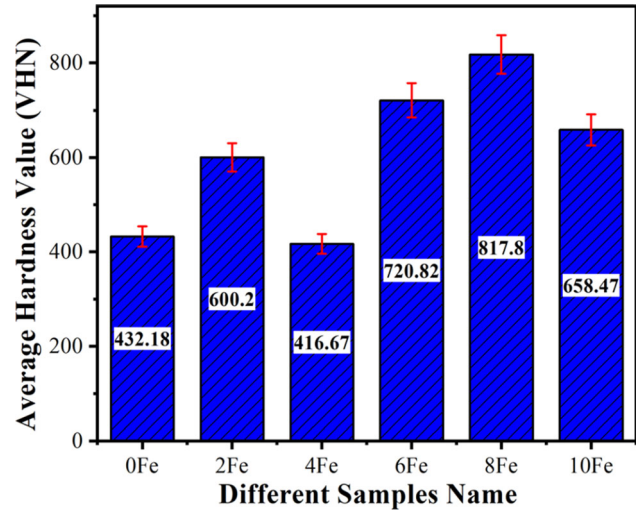


Fig. 12—Vickers hardness value vs different Fe contents.

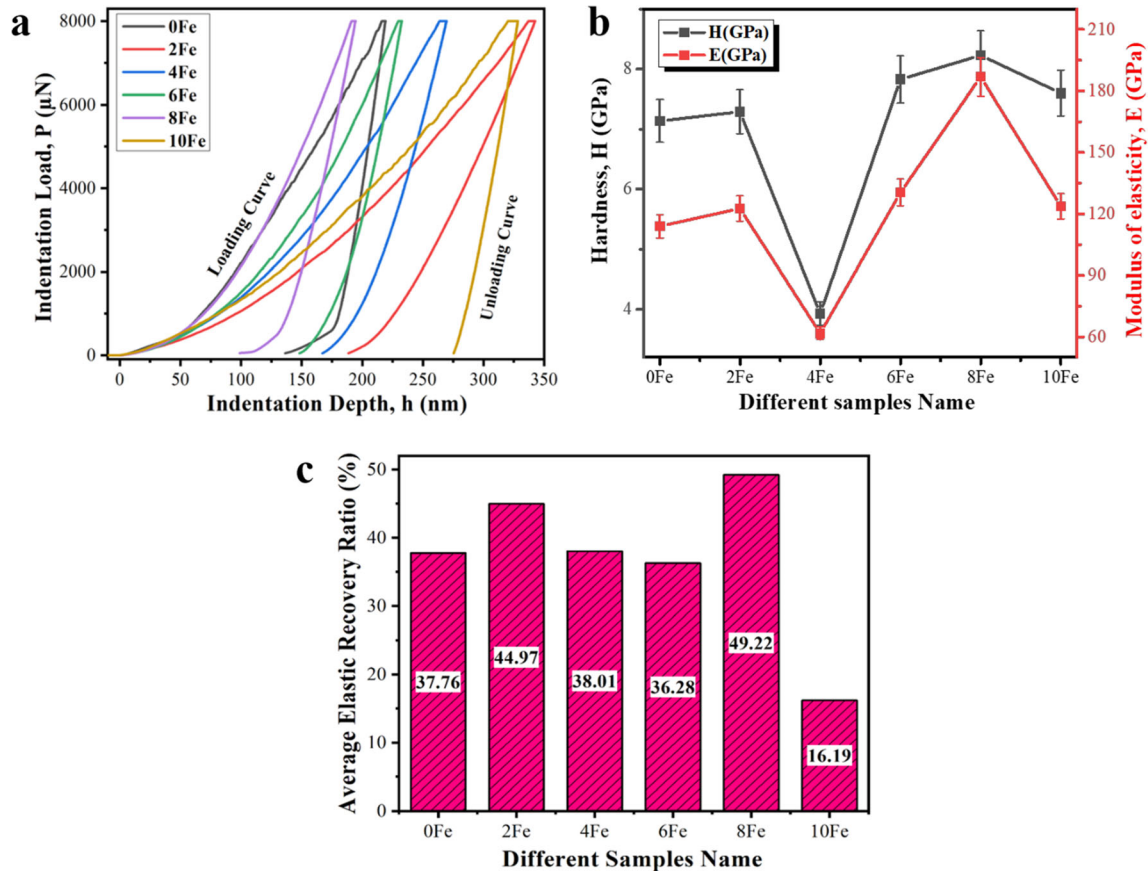


Fig. 11—(a) P-h curve, (b) Elastic modulus and hardness, and (c) Average elastic recovery ratio value for samples with different Fe contents.

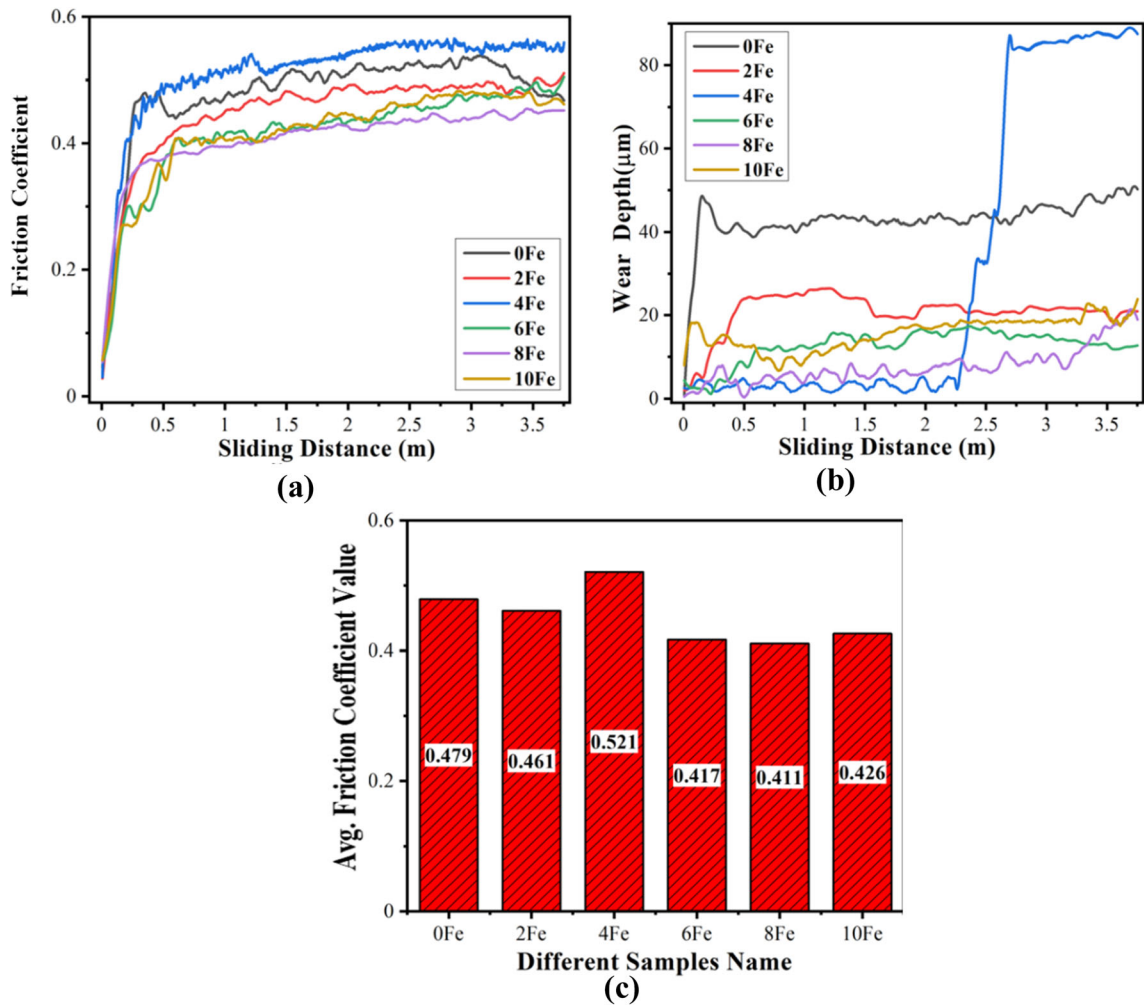


Fig. 13—(a) variation of Friction coefficient, (b) Wear depth vs sliding distance, and (c) Average friction coefficient value vs different sample names.

Figure 13(a) shows the wear debris removed with an increase in the sliding distance. The 8Fe sample has the lowest average coefficient of friction is 0.411, then other compositions owing to the presence of  $\text{Ni}_4\text{Ti}_3$  precipitates, which are shown in Figure 13(c). There is a dependence of the coefficient of friction on the hardness of the surface, and the 8Fe sample is the hardest among the sintered samples. According to Archard's theory, wear resistance is directly dependent on the surface hardness.<sup>[44]</sup> Hence, the 8Fe sample has a better wear resistance than other specimens. There is a sharp increase in the wear depth curve of the 4Fe sample in Figure 13(b), which can be attributed to the removal of precipitates from the surface, leaving behind pores or due to delamination. Therefore, a lower wear depth signifies higher wear resistance and vice versa.

The worn-out surfaces were observed in SEM to study the surface characteristics, as shown in Figure 14. The wear debris generated during the repeating motion gradually moves toward the periphery of the wear track. The mechanism behind wear in the current system can be either due to adhesion or due to abrasion. Specimens having higher hardness values like 8 Fe, 6 Fe, and 10Fe show better resistance to wear. Harder surfaces have a lower tendency for adhesion; the harder the surface, the lower will be the wear. Similarly, 4 Fe, which has a lower hardness, shows a higher coefficient of friction (0.52) and wider wear tracks ( $612.34 \mu\text{m}$ ). Silicon is also detected in the EDS reports in Table V:  $\text{Si}_3\text{Ni}_4$  ceramic ball is used in the sliding motion. The process can also expose the bulk metal to the environment leading to oxidation. Since titanium is present in the alloy, there is

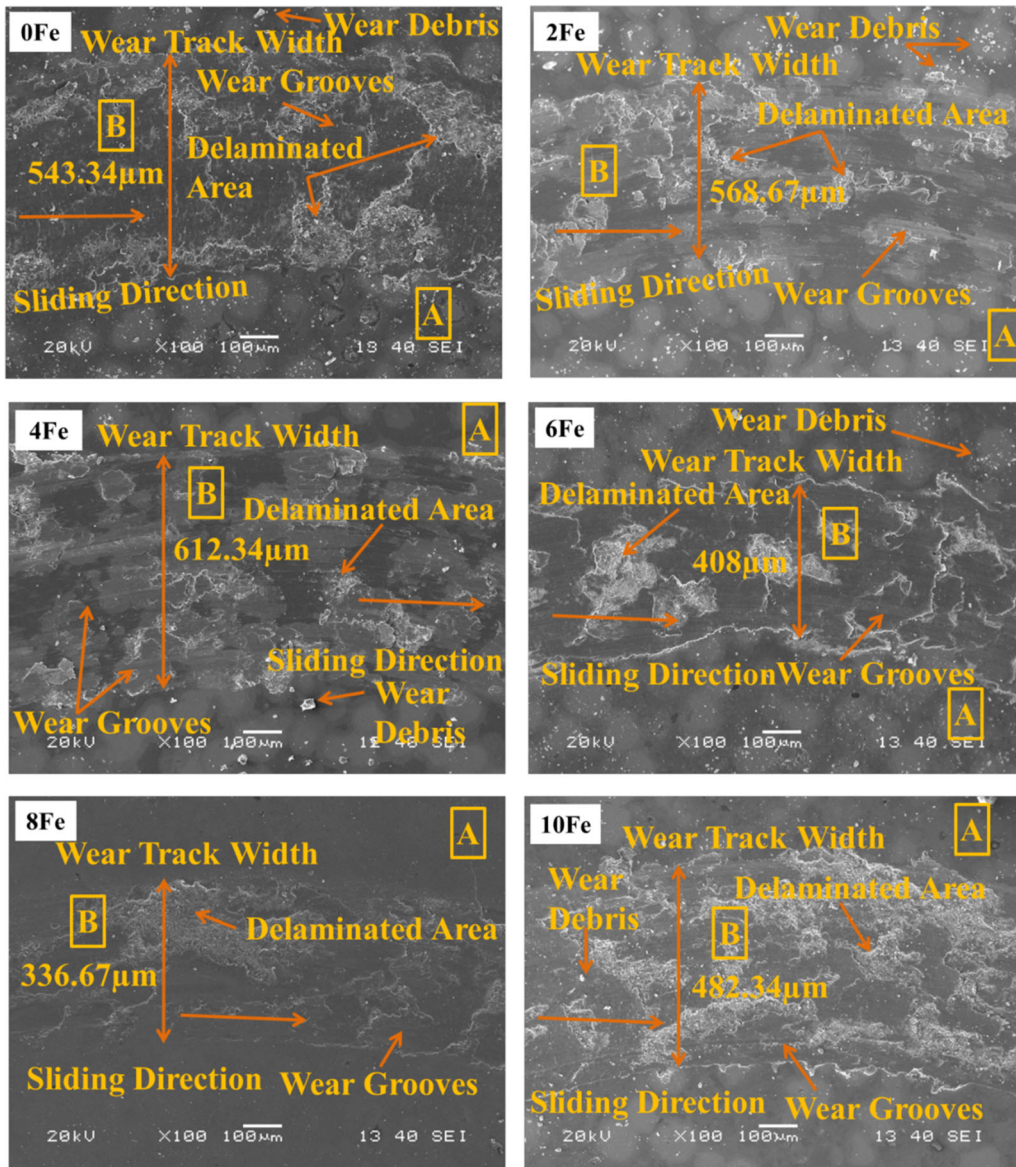


Fig. 14—SEM micrographs of the worn-out surface of different composition samples.

Table V. Chemical Compositions of Wear Track (B) and Outside Wear Track (A) Regions are Marked in Fig. 14

Sample Name	Phase Region	Composition (at. pct)				
		Ni K	Ti K	Fe K	O K	Si K
0Fe	A	33.12	52.46	—	14.42	—
	B	36.73	43.80	—	18.71	0.76
2Fe	A	43.37	31.09	4.81	20.73	—
	B	45.32	26.95	4.18	22.72	0.83
4Fe	A	42.89	31.74	6.74	18.63	—
	B	32.32	41.22	5.12	21.42	0.08
6Fe	A	48.08	23.04	12.02	16.86	—
	B	45.00	23.87	7.35	22.82	0.96
8Fe	A	31.21	31.62	12.45	24.72	—
	B	37.57	21.26	8.74	31.31	1.12
10Fe	A	23.58	35.73	13.57	27.12	—
	B	24.65	37.97	6.92	29.58	0.88

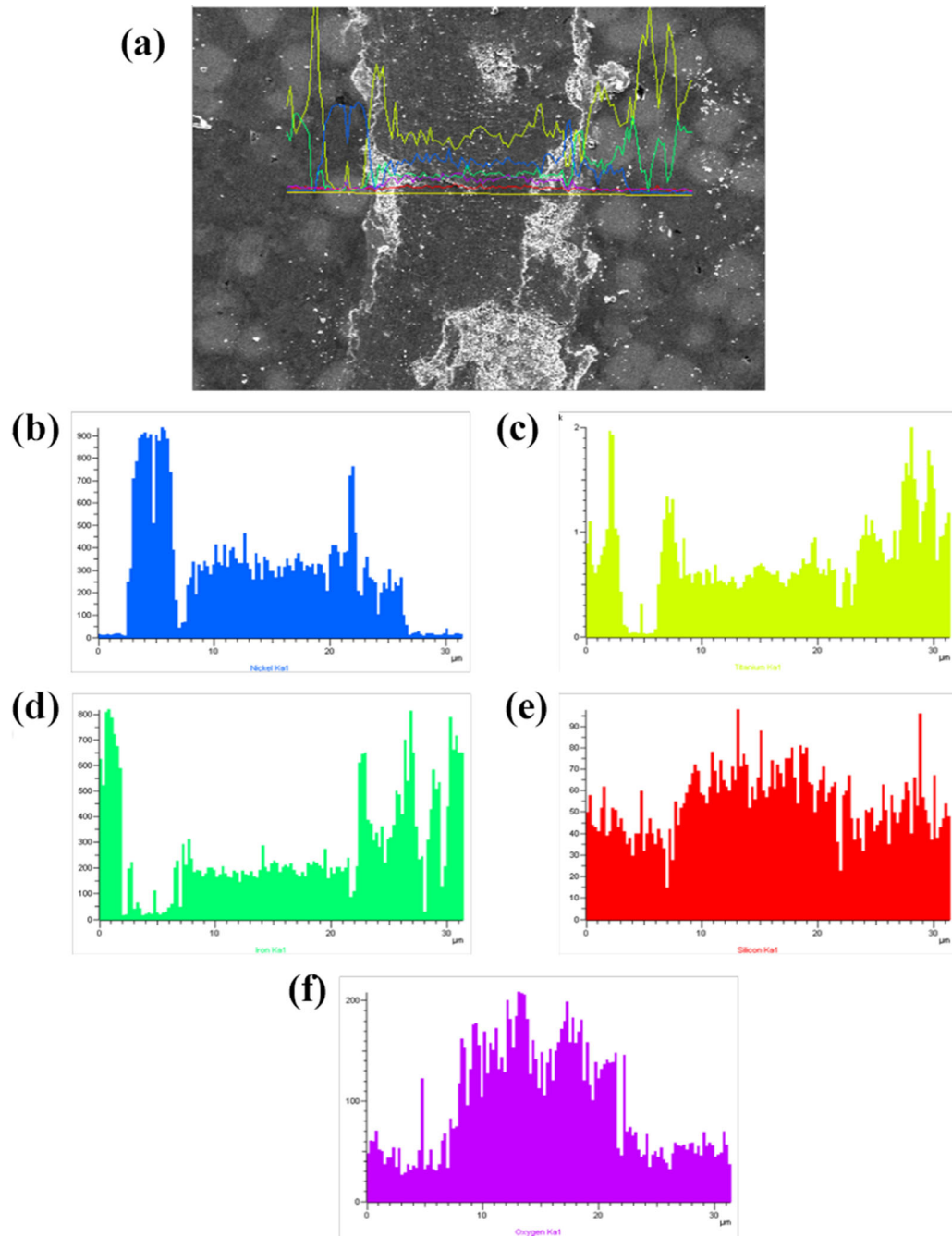


Fig. 15—(a) The line scan analysis of the worn surface of the 10Fe sample in comparison to variation of the element is (b) Ni, (c) Ti, (d) Fe, (e) Si, and (f) O.

always a likelihood of oxidation. The presence of oxygen is prominent at the center of the track (*i.e.*, more oxidation) than at the periphery (*i.e.*, less oxidation), as seen in Figure 15.

Considering all the properties, it is observed that 8Fe has the optimal and best properties among all the prepared samples for shape memory application. The tabular representations of all the properties with the corresponding compositions are shown in Table VI.

#### IV. CONCLUSIONS

The following findings are made for the  $Ti_{50}Ni_{50-x}Fe_x$  sample with the variation of Fe percentage:

- The microstructural and phase analysis of the sample includes collectively the FeNiTi phase and  $\beta$ Ti,  $Fe_2Ti$ , and Ni-rich phases.

**Table VI. Tabular Illustration of Different Compositions and Their Corresponding Properties**

Sample Name	Expt. Density (gm/cc)	Porosity (pct)	Micro-Hardness (HV)	Nanohardness (GPa)	Elastic Modulus (GPa)	Avg. COF	SME (pct)	ERR (pct)
0Fe	6.05	4.91	432.18 ± 21.61	7.14 ± 0.36	113.90 ± 5.70	0.48	1.85	37.76
2Fe	6.08	4.51	600.2 ± 30.01	7.29 ± 0.37	122.61 ± 6.13	0.46	2.29	44.97
4Fe	5.98	5.30	416.67 ± 20.84	3.93 ± 0.20	61.70 ± 3.09	0.52	2.22	38.01
6Fe	6.16	3.56	720.82 ± 36.04	7.83 ± 0.39	130.50 ± 6.53	0.42	1.44	36.28
8Fe	<b>6.19</b>	<b>3.11</b>	<b>817.8 ± 40.89</b>	<b>8.23 ± 0.41</b>	<b>186.87 ± 9.34</b>	<b>0.41</b>	<b>2.79</b>	<b>49.22</b>
10Fe	6.13	3.91	658.47 ± 32.92	7.60 ± 0.38	123.68 ± 6.18	0.43	1.13	16.19

Bold values are for better properties that have been discussed inside the text.

- In comparison to other samples, the 8Fe sample exhibits higher relative density, higher hardness, lower porosity, and higher COF values because it contains more secondary phases, such as Ti<sub>2</sub>Ni, Ni<sub>3</sub>Ti, Fe<sub>2</sub>Ti, and Ni<sub>4</sub>Ti<sub>3</sub>, among others.
- The 8Fe sample shows maximum shape memory effect and elastic recovery, which is because it comprises more amounts of NiTi (B19') martensitic phase than other samples.
- The worn surface of the wear samples exhibits adhesive and abrasive wear mechanisms.
- From all analysis, it is found that there is a dependence of characterization with the variation of Fe content in NiTiFe alloy.

#### ACKNOWLEDGMENTS

This is a part of academic research work and is under the support of the Department of Metallurgical and Materials Engineering, National Institute of Technology, Rourkela, India. The authors are also grateful to Prof. Srinivasa Rao Bakshi, Metallurgical and Materials Engineering Department, Indian Institute of Technology, Madras, for providing spark plasma sintering facilities.

#### CONFLICT OF INTEREST

The authors declare that they have no known competing financial interests or personal relationships that could have appeared to influence the work reported in this paper.

#### REFERENCES

1. Y. Zhao, M. Taya, Y. Kang, and A. Kawasaki: *Acta Mater.*, 2005, vol. 53, pp. 337–43.
2. L.J. Garner, L.N. Wilson, D.C. Lagoudas, and O.K. Rediniotis: *Smart Mater. Struct.*, 2000, vol. 9, pp. 673–83.
3. I. Martynova, V. Skorohod, S. Solonin, and S. Goncharuk: *Le J. Phys. IV*, 1991, vol. 01, pp. 421–26.
4. X.X. Zhang, H.W. Hou, L.S. Wei, Z.X. Chen, W.T. Wei, and L. Geng: *J. Alloys Compd.*, 2013, vol. 550, pp. 297–301.
5. S.A. Hosseini, M. Alizadeh, A. Ghasemi, and M.A. Meshkot: *J. Mater. Eng. Perform.*, 2013, vol. 22, pp. 405–09.
6. G. Chen, P. Cao, G. Wen, N. Edmonds, and Y. Li: *Intermetallics*, 2013, vol. 37, pp. 92–99.
7. J.L. Xu: *Mater. Sci. Eng. C*, 2015, vol. 46, pp. 387–93.
8. T. Habijan: *Mater. Sci. Eng. C*, 2013, vol. 33, pp. 419–26.
9. P. Saravanan, R. Gopalan, D. Sivaprahasam, and V. Chandrasekaran: *Intermetallics*, 2009, vol. 17, pp. 517–22.
10. C. Velmurugan, V. Senthilkumar, K. Biswas, and S. Yadav: *Adv. Powder Technol.*, 2018, vol. 29, pp. 2456–62.
11. O.M. Ozkendir, E. Cengiz, E. Tirasoglu, M. Kaya, I.H. Karahan, and N. Orhan: *J. Mater. Sci. Technol.*, 2013, vol. 29, pp. 344–48.
12. P. Novák, L. Mejlíková, A. Michalčová, J. Čapek, P. Beran, and D. Vojtěch: *Intermetallics*, 2013, vol. 42, pp. 85–91.
13. J. Ryhänen: *J. Biomed. Mater. Res.*, 1998, vol. 41, p. 487.
14. P. Sevilla, C. Aparicio, J.A. Planell, and F.J. Gil: *J. Alloys Compd.*, 2007, vol. 439, pp. 67–73.
15. G. Fan, Y. Zhou, W. Chen, S. Yang, X. Ren, and K. Otsuka: *Mater. Sci. Eng. A*, 2006, vol. 438–40, pp. 622–26.
16. N. Zhou, C. Shen, M.F.X. Wagner, G. Eggeler, M.J. Mills, and Y. Wang: *Acta Mater.*, 2010, vol. 58, pp. 6685–94.
17. H. Xu, J. Chengbao, G. Shengkai, and F. Gen: *Mater. Sci. Eng. A*, 2000, vol. 281(1–2), pp. 234–38.
18. G. Cacciamani, R. Ferro, U.E. Klotz, and J. Lacaze: *Intermetallics*, 2006, vol. 14(10–11), pp. 1312–25.
19. D.Y. Li and R. Liu: *Wear*, 1999, vol. 225–229, pp. 777–83.
20. Y.N. Liang, S.Z. Li, Y.B. Jin, W. Jin, and S. Li: *Wear*, 1996, vol. 198, pp. 236–41.
21. D.Y. Li: *Mater. Des.*, 2000, vol. 21, pp. 551–55.
22. P. Clayton: *Wear*, 1993, vol. 162–164, pp. 202–10.
23. C.A. Zimmerly, O.T. Inal, and R.H. Richman: *Mater. Sci. Eng. A*, 1994, vol. 188(1–2), pp. 251–54.
24. E. Rabinowicz and R.I. Tanner: *J. Appl. Mech.*, 1966, vol. 33, p. 479.
25. C. Zhang and Z.N. Farhat: *Wear*, 2009, vol. 267, pp. 394–400.
26. S.S. Mishra, S.K. Karak, and D. Chaira: *Met. Mater. Int.*, 2021, vol. 27, pp. 4601–17.
27. P. Liu, Q. Kan, and H. Yin: *Mater. Lett.*, 2019, vol. 241, pp. 43–46.
28. C. Velmurugan and V. Senthilkumar: *Mater. Manuf. Process.*, 2019, vol. 34, pp. 369–78.
29. T.S. Huang, S.F. Ou, C.H. Kuo, and C.H. Yang: *Metals*, 2020, vol. 10, p. 527.
30. M. Fellah, M. Abdul Samad, M. Labaiz, O. Assala, and A. Iost: *Tribol. Int. Int.*, 2015, vol. 91, pp. 151–59.
31. M.A. Godinez-Madera: *Mater. Lett.*, 2021, vol. 284, 129010.
32. J. De Keyzer: *Thermodynamic Modeling of the Fe-Ni-Ti System: A Multiple Sublattice Approach*, University of Leuven, Leuven, 2008.
33. S. Wu: *J. Biomed. Mater. Res. Part A*, 2013, vol. 101A, pp. 2586–2601.
34. M.H. Ismail, R. Goodall, H.A. Davies, and I. Todd: *Mater. Lett.*, 2012, vol. 70, pp. 142–45.
35. A.P. Puente and D.C. Dunand: *Intermetallics*, 2018, vol. 92, pp. 42–48.
36. J. Parida, S.C. Mishra, and A. Behera: *Met. Mater. Int.*, 2023, vol. 29, pp. 1145–64.
37. J. Parida, S.C. Mishra, and A. Behera: *Metall. Mater. Trans. A*, 2023, vol. 54, pp. 2585–2604.
38. M. Whitney, S.F. Corbin, and R.B. Gorbet: *Acta Mater.*, 2008, vol. 56, pp. 559–70.
39. C. Shearwood, L. Yu, and K.A. Khor: *Scripta Mater.*, 2005, vol. 52(6), pp. 455–60.
40. M. Farvizi: *Wear*, 2015, vol. 334–335, pp. 35–43.

41. M.L. Young, M. Frotscher, and G. Eggeler: *Int. J. Mater. Res.*, 2012, vol. 103(12), pp. 1434–39.
42. F. Gao and H.M. Wang: *Intermetallics*, 2008, vol. 16, pp. 202–08.
43. L.L. Ye, K. Raviprasad, M.X. Quan, and Z.Q. Hu: *Mater. Sci. Eng. A*, 1998, vol. 241(1–2), pp. 290–93.
44. S. Waqar, A. Wadood, and A. Mateen: *Int. J. Adv. Manuf. Tech.*, 2020, vol. 108, pp. 625–34.

**Publisher's Note** Springer Nature remains neutral with regard to jurisdictional claims in published maps and institutional affiliations.

Springer Nature or its licensor (e.g. a society or other partner) holds exclusive rights to this article under a publishing agreement with the author(s) or other rightsholder(s); author self-archiving of the accepted manuscript version of this article is solely governed by the terms of such publishing agreement and applicable law.